

Journal of Biomedical Optics

SPIEDigitalLibrary.org/jbo

Modified forward model for eliminating the time-varying impact in fluorescence molecular tomography

Wei He
Guanglei Zhang
Huangsheng Pu
Fei Liu
Xu Cao
Jianwen Luo
Jing Bai

Modified forward model for eliminating the time-varying impact in fluorescence molecular tomography

Wei He,^{a,†} Guanglei Zhang,^{a,†} Huangsheng Pu,^a Fei Liu,^a Xu Cao,^b Jianwen Luo,^{a,c} and Jing Bai^{a,*}

^aTsinghua University, School of Medicine, Department of Biomedical Engineering, Beijing 100084, China

^bXidian University, School of Life Sciences and Technology, Xi'an 710071, China

^cTsinghua University, Center for Biomedical Imaging Research, Beijing 100084, China

Abstract. In conventional fluorescence molecular tomography, the distribution of fluorescent contrast agents is reconstructed with the assumption of constant concentration during data acquisition for each image frame. However, the concentration of fluorescent contrast target is usually time-varying in experiments or *in-vivo* studies. In this case, the reconstruction methods cannot be directly applied to the fluorescence measurements without considering the time-varying effects of concentration. We propose a modified forward model by dividing the fluorescence yield distribution into two parts: one is a constant representing the spatial distribution of the fluorescent target and the other is an impact factor representing the effects of the concentration change and other possible factors. By extracting spatial distribution information from the reconstruction result, the location and volume of the fluorescent target can be obtained accurately. Both simulation and phantom experiments are carried out and the results indicate that, by using the modified forward model, the quality of reconstruction could be significantly improved in terms of accurate localization and strong anti-noise ability. © 2014 Society of Photo-Optical Instrumentation Engineers (SPIE) [DOI: [10.1117/1.JBO.19.5.056012](https://doi.org/10.1117/1.JBO.19.5.056012)]

Keywords: fluorescence molecular tomography; forward model; image reconstruction; time-varying.

Paper 140137R received Mar. 3, 2014; revised manuscript received Apr. 19, 2014; accepted for publication May 5, 2014; published online May 22, 2014.

1 Introduction

Fluorescence molecular tomography (FMT) is an important molecular imaging modality developed to reveal three-dimensional (3-D) distribution of the fluorescent targets using fluorescence measurements and appropriate image reconstruction methods. It has the advantages of low cost, high sensitivity, noninvasiveness, and no ionization radiation.¹⁻³ During the past years, FMT has made significant progress with developments in imaging systems,⁴⁻⁶ mathematical models,⁷⁻¹⁰ and fluorescent agents.¹¹ FMT has been extensively applied to visualization of biological and medical processes *in vivo* at cellular and molecular levels and provides a powerful technical tool for disease detection, drug discovery, etc.¹²⁻¹⁴

Conventionally, the images of FMT are reconstructed based on the (implicit) assumption that the fluorophore concentration is constant during the acquisition process of measurement data for each image frame.¹⁻³ The temporal resolution of FMT is about 1 to 2 min depending on the sum of rotation time and total exposure time of projection images.¹⁵⁻¹⁷ The assumption holds even in advanced reconstruction methods that attempt to obtain dynamic FMT images frame by frame.¹⁶⁻²⁰

However, many reports have demonstrated that the concentration of fluorescent target is time-varying in experiments or *in-vivo* studies due to physical degradation of fluorophores²¹ (photodegradation, thermal degradation, etc.) or the process of metabolism,²² which means that the concentration may exhibit significant changes during the time of measurement data

acquisition for one image frame.^{16,17,22} In this case, if the reconstruction methods are directly applied to the fluorescence measurements without considering the time-varying effects of concentration, inaccurate localization of fluorescent target and a high level of noise will be obtained.^{23,24} To acquire high quality reconstruction results, the time-varying information of the concentration should be taken into account.

In this study, we propose a modified forward model based on the compartment model theory,¹⁸ a well-known approach for pharmacokinetic analysis, to eliminate the impacts due to the concentration change of fluorescent targets. In this model, the unknown fluorescence yield distribution is divided into two parts. One part is a constant representing the spatial distribution (location and volume) of the fluorescent target and the other is an impact factor representing the effects of the concentration change and other possible factors. This is because the concentration of fluorescent targets in the region of interest (ROI) may vary significantly with time, but the location and volume of the ROI filled with fluorescent targets remains invariant. Based on the modified model, a new linear relationship between the unknown and the boundary measurement can be constructed, from which an accurate and constant spatial distribution of the fluorescent target can be obtained with Tikhonov regularization. Simulation studies and phantom experiments are conducted to qualitatively and quantitatively illustrate the improvement in the localization of fluorophore and anti-noise abilities with the proposed model.

The outline of this paper is as follows. In Sec. 2, the details of the proposed model are described. The materials used in the

*Address all correspondence to: Jing Bai, E-mail: deabj@tsinghua.edu.cn

[†]These authors contributed equally to this work.

simulation studies and phantom experiments are described in Sec. 3. In Sec. 4, the reconstruction results are presented to show the performance of the proposed model. Finally, discussions and conclusion are provided in Sec. 5.

2 Method

2.1 Conventional Forward Model

A suitable model for photon propagation plays a crucial role in fluorescence tomographic reconstruction. Diffusion equation (DE), as an approximation to the radiative transfer equation, has been successfully used to describe the light transport in the near-infrared spectral window.²⁵ For FMT, coupled DEs, which describe the photon migration in the excitation and emission spectrum, can be written as follows:²⁶

$$\begin{cases} -\nabla \cdot [D_x(\mathbf{r})\nabla\Phi_x(\mathbf{r})] + \mu_{ax}(\mathbf{r})\Phi_x(\mathbf{r}) = s(\mathbf{r}) \\ -\nabla \cdot [D_m(\mathbf{r})\nabla\Phi_m(\mathbf{r})] + \mu_{am}(\mathbf{r})\Phi_m(\mathbf{r}) = \Phi_x(\mathbf{r})x(\mathbf{r}) \end{cases}, \quad (1)$$

where the subscripts x and m denote the excitation and emission wavelengths, respectively; $s(\mathbf{r})$ is the excitation source; $D_{x,m}$ is the diffusion coefficient given by $D_{x,m} = 1/3[\mu'_{sx,m}(\mathbf{r}) + \mu_{ax,m}(\mathbf{r})]$, where $\mu'_{sx,m}(\mathbf{r})$ is the reduced scattering coefficient; $\mu_{ax,m}(\mathbf{r})$ stands for the absorption coefficient of the medium; $\Phi_{x,m}(\mathbf{r})$ represents the photon flux density; $x(\mathbf{r})$ denotes the fluorescence yield, which is directly proportional to the fluorophore concentration.²⁷

The corresponding Robin-type boundary condition²⁵ is given by

$$\Phi_{x,m}(\mathbf{r}) + 2\rho D_{x,m}(\mathbf{r}) \frac{\partial\Phi_{x,m}(\mathbf{r})}{\partial\mathbf{n}} = 0, \quad (2)$$

where \mathbf{n} denotes the outward normal of the boundary and ρ is the boundary mismatch parameter and accounts for the light reflection on the boundary surface.

In this paper, the absorption coefficient and reduced scattering coefficient are assumed to be the same at the excitation and emission wavelengths, which is reasonable because the excitation and emission wavelengths are close to each other.²⁸

In the finite element framework,²⁹ a linear relationship between the unknown fluorescence distribution and the boundary measurements of the s 'th projection can be constructed as

$$\mathbf{W}_s \mathbf{x}_s = \Phi_s \quad (s = 1, 2, \dots, L), \quad (3)$$

where L is the number of projections for one image frame. $\mathbf{W}_s = (\mathbf{W}_{s,d})$ is the subsystem matrix, which is composed of the mapping vector of all source-detect pairs in the s 'th projection. $\Phi_s = [\Phi(r_s)]$ is the vector composed of the fluorescence data of the s 'th projection. \mathbf{x}_s is the distribution of the fluorescence in the s 'th projection.

In the conventional FMT, the concentration of the fluorescent target is assumed to be constant during data acquisition for one image frame. It means that \mathbf{x}_s is constant at all the projections ($s = 1, 2, \dots, L$). Thus, the final system equation of FMT can be constructed with the subsystem equations of all the projections

$$\mathbf{W}\mathbf{x} = \Phi, \quad (4)$$

where \mathbf{x} is an $N \times 1$ vector representing the fluorescent probe distribution to be reconstructed. Φ is an $M \times 1$ vector which contains the emission measurements at the boundary based on charge-coupled device (CCD) camera photon detection, and \mathbf{W} is an $M \times N$ weight matrix.

2.2 Modified Forward Model

As described in Sec. 1, \mathbf{x}_s is usually time-varying during measurement data acquisition at different projections. It means the final system equation cannot be obtained by directly combining the subsystem equations together.

In the modified forward model, \mathbf{x}_s consists of two components as follows:

$$\mathbf{x}_s = k_s * \mathbf{x}_0, \quad (5)$$

where \mathbf{x}_0 is an $N \times 1$ vector representing the spatial distribution of the fluorescent targets. Here, the spatial distribution specifically refers to the location and volume of the fluorescent target, which is changeless with all the projections. k_s ($s = 1, 2, \dots, L$) is defined as an impact factor in the s 'th projection ($k_s > 0$), representing the effects of the concentration change and other possible factors.

Then, the new subsystem equation can be obtained by substituting Eq. (5) into Eq. (3):

$$\mathbf{W}_s * \mathbf{x}_0 = \frac{\Phi_s}{k_s}. \quad (6)$$

In order to make the mathematical solution possible, we define k_s as

$$k_s = \frac{1}{1 - p_s} \quad (p_s < 1), \quad (7)$$

where p_s is meaningless in physics. For simplicity, p_s is used to indicate the impact factor in the following part of this paper.

By substituting Eq. (7) into Eq. (6), we obtain

$$\mathbf{W}_s * \mathbf{x}_0 + \Phi_s * p_s = \Phi_s. \quad (8)$$

Thus, we can obtain the modified system matrix of FMT from Eq. (8)

$$\mathbf{A} = \begin{pmatrix} \mathbf{W}_1 & \Phi_1 & & \mathbf{0} \\ \vdots & & \ddots & \\ \mathbf{W}_s & & & \Phi_s \\ \vdots & & & \\ \mathbf{W}_L & \mathbf{0} & & \Phi_L \end{pmatrix}. \quad (9)$$

Then, the new unknown composed of the spatial distribution of the fluorescent target and the impact factor can be written as

$$\mathbf{y} = \begin{pmatrix} \mathbf{x}_0 \\ \mathbf{p} \end{pmatrix}, \quad (10)$$

where $\mathbf{p} = (p_1, p_2, \dots, p_L)$ is an $L \times 1$ vector and \mathbf{y} is an $(N + L) \times 1$ vector.

The final system equation of the FMT can be written as

$$\mathbf{A} * \mathbf{y} = \Phi, \quad (11)$$

where Φ is still an $M \times 1$ vector and \mathbf{A} is an $M \times (N + L)$ weight matrix. After extracting spatial distribution information \mathbf{x}_0 from \mathbf{y} , the location and volume of the fluorescent target can be obtained.

2.3 Tikhonov Regularization

For Eqs. (4) or (11), the estimation of \mathbf{x} or \mathbf{y} from the measurement vector Φ is an ill-posed inverse problem due to the highly diffusive nature of the photon propagation in tissues.²⁹ Here, the Tikhonov regularization method³⁰ is implemented to address this problem, as it could often provide a reasonable solution and could be efficiently solved by now-standard minimization tools. In the time-varying case as described by Eq. (11), the objective function can be stated as

$$\mathbf{E}(\mathbf{y}) = \|\Phi - \mathbf{A}\mathbf{y}\|^2 + \lambda\|\mathbf{L}\mathbf{y}\|^2, \quad (12)$$

where λ is the regularization parameter ($\lambda > 0$) and is empirically set, and \mathbf{L} is an $(N + L) \times (N + L)$ identity regularization matrix.

By minimizing the objective function $\mathbf{E}(\mathbf{y})$ given in Eq. (12) with respect to \mathbf{y} , the fluorescence distribution [i.e., \mathbf{x}_0 in Eq. (10)] can be obtained. The minimization of $\mathbf{E}(\mathbf{y})$ is performed using the least-squares algorithm.³¹ The process for solving Eq. (4) is the same as that for Eq. (11).

2.4 Evaluation Metrics

In this paper, the contrast-to-noise ratio (CNR)³² and relative error (RE) are selected as the evaluation indices to quantitatively assess the quality of the reconstructed images.

The contrast of the regions with the fluorescent target to the background can be quantified by the CNR, and a higher CNR implies a better image quality. Given an ROI where the fluorescent target is confined, the CNR is defined by

$$\text{CNR} = \frac{\mu_{\text{ROI}} - \mu_{\text{BCK}}}{(\omega_{\text{ROI}}\sigma_{\text{ROI}}^2 + \omega_{\text{BCK}}\sigma_{\text{BCK}}^2)^{1/2}}, \quad (13)$$

where μ_{ROI} and μ_{BCK} are the mean fluorophore concentration values in the ROI and background, respectively; σ_{ROI}^2 and σ_{BCK}^2 are the variances in the ROI and background, respectively; ω_{ROI} and ω_{BCK} are the weighting factors determined by the relative volumes of the ROI and background, respectively.

The RE can comprehensively quantify the reconstruction accuracy and a smaller RE implies a better image quality. The RE is defined as

$$\text{RE} = \frac{\|X - X_{\text{actual}}\|}{\|X_{\text{actual}}\|}, \quad (14)$$

where X_{actual} is the actual distribution of the fluorescent target and X is the reconstruction result.

3 Materials

3.1 Simulation Studies

In the simulation studies, a virtual mouse atlas was employed to provide the 3-D anatomical information.^{33,34} We focused on imaging the kinetic behaviors of indocyanine green (ICG) in the lungs and liver, and the mouse torso from the neck to the base of the liver was selected as the investigated region, with a length of 2.9 cm. The rotational axis of the mouse was defined as the Z-axis with the bottom plane set as $Z = 0$ cm.

To simulate the photons' propagation in biological tissues, a heterogeneous mouse model was set up. It was composed of the heart, lungs, liver, and kidneys, as shown in Fig. 1(a). The optical parameters from Ref. 35 were assigned to the corresponding organs. To simplify the problem, optical properties outside the organs were regarded as homogeneous.

With the image model, the time course of ICG as it circulated in the lungs and liver following the tail vein injection was simulated. The true time course of ICG in the lungs and liver was obtained from Ref. 22 and is shown in Fig. 1(b). Twenty-four projections evenly distributed over 360 deg were used to acquire the measurement data of one image frame. The speed of the rotation stage was set to 6 deg/s and the CCD exposure time in each projection was 0.5 s. Thus, the interval of each projection was 3 s and the time resolution of the FMT system was about 72 s. Here, two periods in the time course of ICG were selected: one from 1000 to 1072 s, when the concentrations of ICG in the lungs and liver are in a nearly steady state within 24 projections [case 1 in Fig. 1(b)]; the other from 60 to 132 s, when the concentrations of ICG in the lungs and liver are in a steep rise period [case 2 in Fig. 1(b)].

3.2 Phantom Experiments

The performance of the proposed model was further evaluated in phantom experiments based on a noncontact full-angle FMT

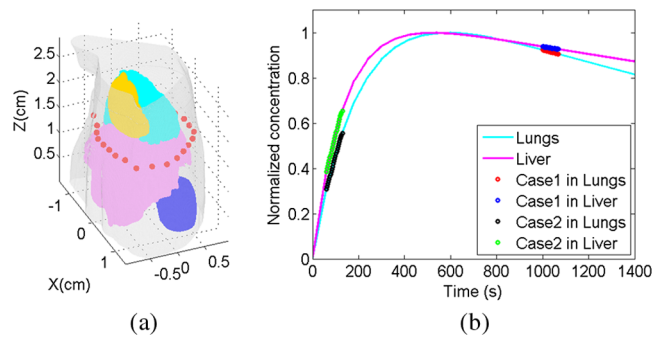


Fig. 1 Schematic diagram of the simulation model. (a) The three-dimensional (3-D) geometric model of the digital mouse used in the simulations with a length of 2.9 cm from the neck to the base of the liver (surface: gray; heart: yellow; lungs: cyan; liver: pink; and kidneys: purple). The red points in (a) indicate the position ($Z = 1.5$ cm) of 24 isotropic point sources. For each excitation source, the fluorescence is measured from the opposite side within a 160 field-of-view. (b) Time course of ICG in the lungs and liver. The cyan and pink curves are the actual time course of ICG in the lungs and liver, respectively, which are obtained from Ref. 22. Case 1 (lungs: red point and liver: blue point) represents the concentration of ICG in a nearly steady state (from 1000 to 1072 s). Case 2 (lungs: black point and liver: green point) represents the concentration of ICG in a steep rise period (from 60 to 132 s).

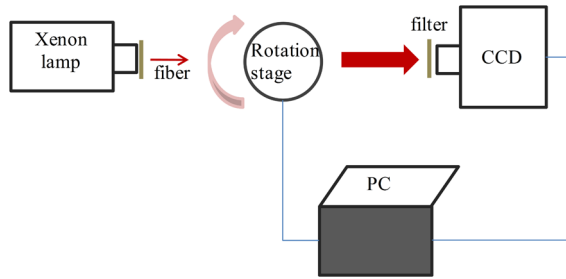


Fig. 2 The schematic of the noncontact full-angle fluorescence molecular tomography system.

system previously developed by our laboratory.³⁶ The sketch of the system is shown in Fig. 2. Briefly, the imaged object was placed on a 360 deg rotation stage working under a step-by-step mode. Around the rotational stage, a noncontact full-angle FMT system was positioned to acquire the fluorescence measurement data.

Figure 3 shows the schematic diagram of the phantom experiments. A glass cylinder (3.0 cm in diameter and 4.5 cm in height) filled with a mixture of water and intralipid was employed as the homogeneous phantom ($\mu_a = 0.02 \text{ cm}^{-1}$ and $\mu_s' = 10.0 \text{ cm}^{-1}$). Two small transparent glass tubes (0.5 cm in diameter) filled with different concentrations of ICG were immersed in the cylinder phantom and used as the fluorescent targets. A point excitation source was located at approximately half the height of the phantom. For the acquisition of the fluorescence images, a $775 \pm 6 \text{ nm}$ excitation filter and an $840 \pm 6 \text{ nm}$ emission filter were separately placed in the front of the point excitation source and the CCD camera.

During the data acquisition process, the phantom was placed on the rotation stage and rotated for 360 deg. For the whole circle, 18 fluorescence images were acquired with an angular increment of 20 deg. In each projection angle, the two tubes shown in Fig. 3(b) were both filled in ICG with the predefined concentrations shown in Fig. 3(c), and one fluorescence image was acquired. After finishing the data acquisition of a projection angle, the cylinder phantom was rotated to the next projection angle, the two tubes were filled in ICG with the next predefined concentrations shown in Fig. 3(c), and another fluorescence image was acquired for the new projection angle. The curves shown in Fig. 3(c) were the predefined concentrations of the

two fluorescent targets in the phantom experiments, and were used to imitate the time-varying ICG concentrations of the mouse lungs and liver in the steep rise period (case 2 of the simulation studies) described in Sec. 3.1. For simplicity, the concentrations of the two fluorescent targets were set to increase linearly in the 18 projection angles because the concentrations of the mouse lungs and liver in case 2 of the simulation studies also increased approximate linear.

4 Results

All computations in this paper were carried out on a personal computer with Intel(R) Core(TM) i7 CPU (2.80 GHz) and 8 GB RAM. In the simulation studies and phantom experiments, the reconstruction results of the spatial distribution \mathbf{x}_0 were shown while the impact factor \mathbf{p} was not provided because this work focused on obtaining accurate locations and volumes of the fluorescent targets. Since the locations and volumes of the fluorescent targets should be the same under different time-varying concentration situations, the spatial distribution \mathbf{x}_0 , which represented the locations and volumes of the fluorescent targets, was normalized by its maximum in both the simulation studies and phantom experiments.

4.1 Reconstruction Results of Simulations

The reconstruction results based on the conventional and modified forward models in the simulation studies are illustrated in Figs. 4 and 5. The results are normalized by the maximum and presented in the form of the sections. The two red solid lines on the 3-D image indicate the positions of the two investigated section images which are the representative slices of the lungs and the liver, respectively. In both Figs. 4 and 5, (b) and (e) are the actual distributions of the fluorescent targets, (c) and (f) are the reconstruction results based on the conventional forward model, and (d) and (g) are the reconstruction results based on the modified forward model.

Figure 4 shows the results of case 1, where the concentrations of ICG in the lungs and liver are in a nearly steady state within 24 projections. For this case, both models could obtain high quality results with accurate locations of the fluorescent targets and small noise level. Table 1 shows the quantitative results of case 1. The CNR and RE of the reconstruction results obtained by the two models are similar to each other. In addition, the computational times of the two models are also similar to each other.

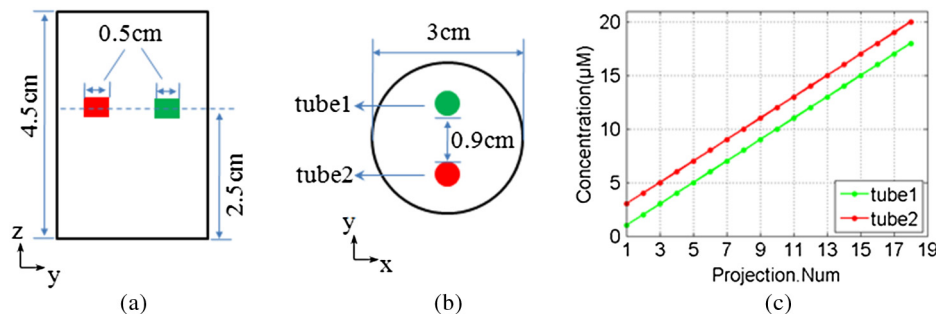


Fig. 3 The schematic diagram of the phantom experiments. (a) The side view of the phantom. (b) The top view of the phantom. A glass cylinder (3.0 cm in diameter and 4.5 cm in height) containing a mixture of water and intralipid was employed as the phantom. Two transparent glass tubes (0.5 cm in outer diameter) filled with different concentrations of ICG in each projection were immersed into the phantom to serve as the fluorescent targets. (c) ICG concentration curves in the two tubes. Each point in (c) denotes the ICG concentration in each projection.

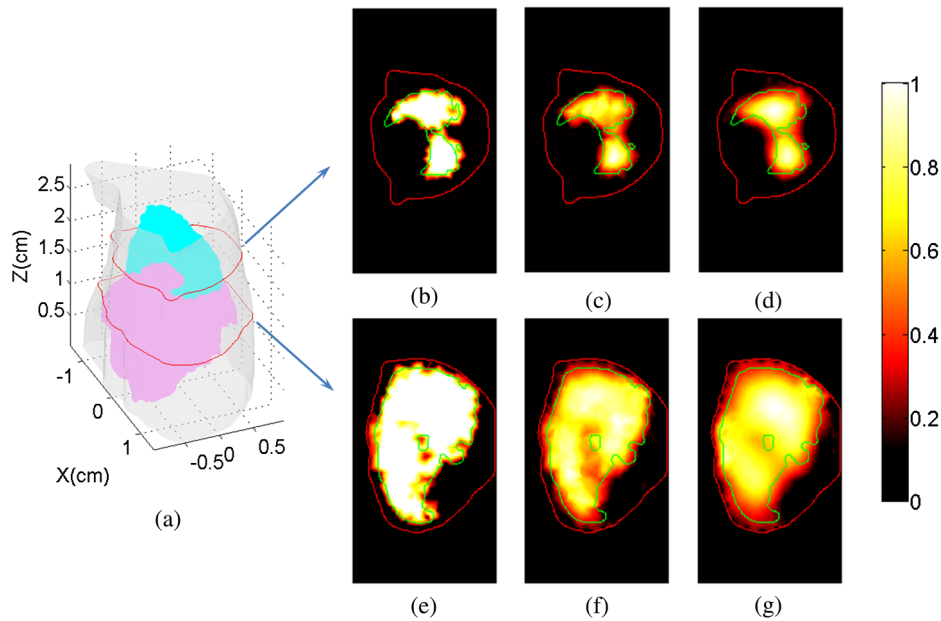


Fig. 4 The reconstruction result of case 1 in the simulation studies. (a) Schematic diagram of the simulation model. (b and e) The actual spatial distribution of the fluorescent targets. (c and f) The reconstruction results based on the conventional forward model. (d and g) The reconstruction results based on the modified forward model. Panels (b)–(d) are the representative slice of the lungs and panels (e)–(g) are the representative slice of the liver. All the reconstructed images are normalized by the maximum of the results.

Figure 5 shows the results of case 2, where the concentrations of ICG in the lungs and liver are in a steep rise period. Due to the significant change of concentrations, the reconstruction results based on the conventional forward model show inaccurate locations and volumes of the fluorescent targets, and suffer from a high level of noise [see Figs. 5(c) and 5(f)]. In contrast,

a significant improvement in locations and volumes of the fluorescent targets and anti-noise ability is obtained with the modified forward model [see Figs. 5(d) and 5(g)]. Table 1 also shows the quantitative results of case 2. It can be seen that the CNR obtained with the modified model is higher than that with the conventional model, while the RE obtained

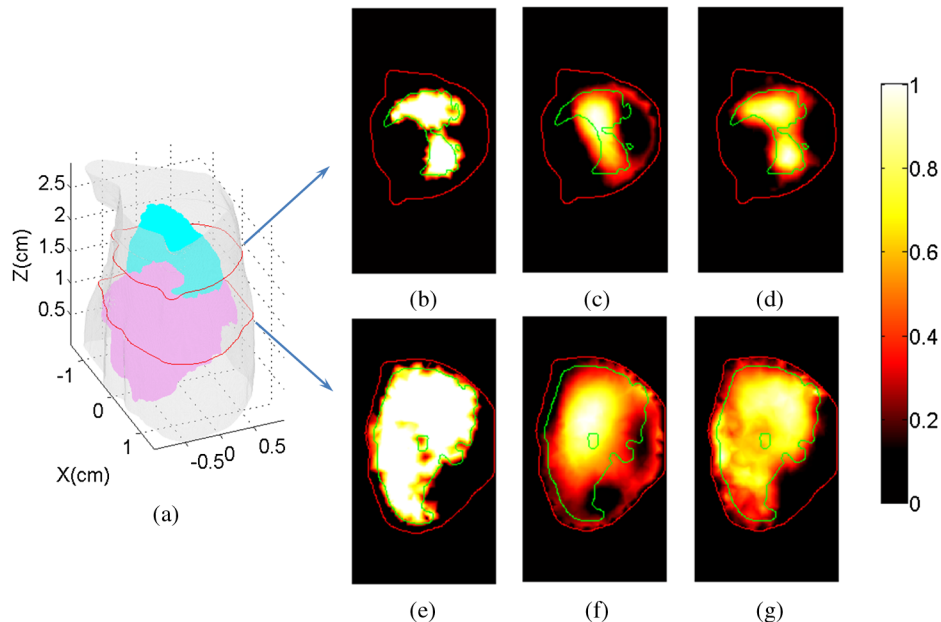


Fig. 5 The reconstruction result of case 2 in the simulation studies. (a) Schematic diagram of the simulation model. (b and e) The actual spatial distribution of the fluorescent targets. (c and f) The reconstruction results based on the conventional forward model. (d and g) The reconstruction results based on the modified forward model. Panels (b)–(d) are the representative slice of the lungs and panels (e)–(g) are the representative slice of the liver. All the reconstructed images are normalized by the maximum of the results.

Table 1 Quantitative analysis of the reconstruction results in the simulation studies.

	Model	Contrast-to-noise ratio (CNR)	Relative error (RE)	Time (s)
Case 1	Conventional	3.77	0.31	40.9
	Modified	4.52	0.27	41.7
Case 2	Conventional	1.47	0.87	41.1
	Modified	3.33	0.41	42.3

with the modified model is smaller than that with the conventional model. The computational times of the two models are similar to each other.

4.2 Reconstruction Results of Phantom Experiments

The reconstruction results based on the conventional and modified forward models in the phantom experiments are illustrated in Fig. 6. The reconstruction results are normalized by the maximum and presented in the form of the sections and 3-D views. The red solid line on the 3-D image indicates the position of the investigated section image. Figures 6(a) and 6(d) are the actual fluorescent targets. Figures 6(b) and 6(e) are the reconstruction results based on the conventional forward model. Figures 6(c) and 6(f) are the reconstruction results based on the modified forward model.

Due to the significant change of ICG concentration in the tube, the reconstruction results based on the conventional forward model show wrong locations and volumes of the fluorescent targets, and suffer from a high level of noise

Table 2 Quantitative analysis of the reconstruction results in the phantom experiments.

Model	CNR	RE	Time (s)
Conventional	4.91	1.11	49.8
Modified	8.63	0.34	50.9

[Figs. 6(b) and 6(e)]. On the contrary, accurate locations and volumes of the fluorescent targets and less noisy results are obtained with the proposed model [Figs. 6(c) and 6(f)]. Table 2 shows the quantitative results of the phantom experiments. The CNR of the reconstruction results obtained with the modified model is significantly higher than that with the conventional model. The RE obtained with the modified model is much smaller than that with the conventional model. The computational times of the two models are similar to each other.

5 Discussion

FMT plays an important role in revealing biological processes *in vivo* by 3-D visualization of fluorescent targets. However, when the concentrations of the fluorescent targets are time-varying during data acquisition for one image frame, the reconstruction of FMT based on the assumption of constant fluorophore concentration could not obtain accurate locations and volumes of the fluorescent targets, but instead bring a lot of noise into the results. The main aim of this paper is to improve the performance of FMT when the concentrations of the fluorescent targets exhibit significant changes during data acquisition. This is achieved with a modified forward model, which divides the fluorescence yield distribution into two parts. \mathbf{x}_0 is a constant

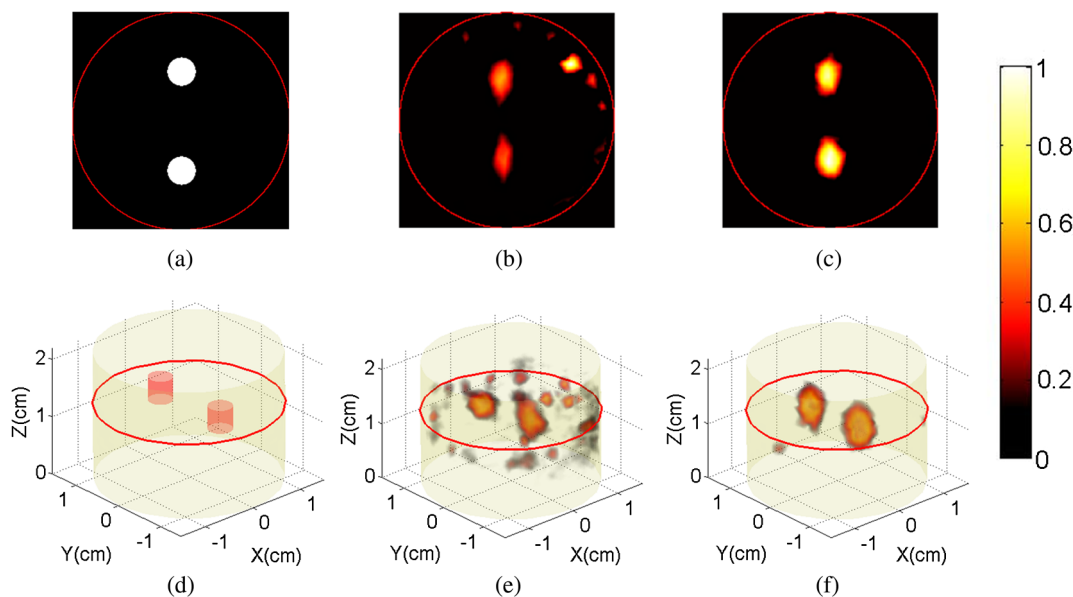


Fig. 6 Sections and 3-D views of the reconstruction result in the phantom experiments. (a and d) The actual fluorescent targets. (b and e) The reconstruction result based on the conventional forward model. (c and f) The reconstruction result based on the modified forward model. The red solid line on the 3-D image (d–f) indicates the position of the investigated two-dimensional image (a–c). All the images are normalized by the maximum of the results.

representing the spatial distribution of the fluorescent target and k_s is an impact factor representing the effects of the concentration change and other possible factors. Based on the modified forward model, a new linear relationship between the unknown and the boundary measurement ($\mathbf{A} * \mathbf{y} = \Phi$) can be constructed for reconstruction. Afterward, the spatial distribution \mathbf{x}_0 can be exacted from the reconstruction result \mathbf{y} .

In the simulations, when the concentrations of ICG in the lungs and liver are nearly constant within different projections during data acquisition [case 1 in Fig. 1(b)], high quality results [Figs. 4(c) and 4(f)] could be obtained with both the conventional and modified forward models. In particular, the difference between the reconstruction results obtained with both models could be neglected [see Fig. 4 and Table 1 (case 1)]. This suggests that the reconstruction based on both models is appropriate for the case with time-invariant concentrations of fluorescent targets.

Nevertheless, when the fluorophore concentrations severely change at different projections, the reconstruction based on the conventional forward model would be seriously affected. Figures 5(c), 5(f), 6(b), and 6(e) showed that the reconstruction results suffered from a high level of noise, and a very serious deviation both in the locations and volumes of the fluorescent targets, in both simulations and phantom experiments. In contrast, the results in Figs. 5(d), 5(g), 6(c), and 6(f) demonstrated that the modified forward model could significantly improve the localization and anti-noise capability of the reconstruction. In addition, the quantitative results of CNRs and REs in Tables 1 (case 2) and 2 also illustrated a higher image quality by using the proposed model.

It should be noted that this work focuses on obtaining an accurate spatial distribution \mathbf{x}_0 which represents the locations and volumes of the fluorescent targets, rather than the time-varying concentrations of the fluorescent targets, because the scale factor k_s is a single value which represents the overall effects of the concentration change. In order to obtain the time-varying concentration curves, k_s should be made spatially varying and it will become a vector with the same length as \mathbf{x}_0 . This will significantly aggravate the ill-posedness of the FMT inverse problem, since the number of unknowns is doubled. Nevertheless, with the time-varying concentration curves obtained, the proposed modified model will be further perfected. Furthermore, the kinetic parameters which have significant physiological and pathological meanings can also be estimated by analyzing the time-varying concentration curves.^{37,38}

In conclusion, we proposed a modified forward model for the case with fluorophore concentration changes during the acquisition process of measurement data, which could significantly improve the quality of the reconstruction in terms of accurate localization and strong anti-noise ability. Reconstruction results of both simulation and phantom studies have verified the effectiveness of the proposed model. Future work will focus on validation of this model in *in-vivo* experiments.

Acknowledgments

This work is supported by the National Basic Research Program of China (973) under Grant No. 2011CB707701; the National Natural Science Foundation of China under Grant Nos. 81227901, 81271617, 61322101, and 61361160418; the National Major Scientific Instrument and Equipment Development Project under Grant No. 2011YQ030114.

References

1. V. Ntziachristos et al., "Looking and listening to light: the evolution of whole-body photonic imaging," *Nat. Biotechnol.* **23**, 313–320 (2005).
2. V. Ntziachristos, "Going deeper than microscopy: the optical imaging frontier in biology," *Nat. Methods* **7**, 603–614 (2010).
3. G. Luker and K. Luker, "Optical imaging: current applications and future directions," *J. Nucl. Med.* **49**(1), 1–4 (2007).
4. V. Ntziachristos et al., "In vivo tomographic imaging of near-infrared fluorescent probes," *Mol. Imaging* **1**(2), 82–88 (2002).
5. G. Hu, J. Yao, and J. Bai, "Full-angle optical imaging of near-infrared-fluorescent probes implanted in small animals," *Prog. Nat. Sci.* **18**(6), 707–711 (2008).
6. T. Lasser and V. Ntziachristos, "Optimization of 360° projection fluorescence molecular tomography," *Med. Image Anal.* **11**(4), 389–399 (2007).
7. K. Ren, G. Bal, and A. H. Hielscher, "Transport- and diffusion-based optical tomography in small domains: a comparative study," *Appl. Opt.* **46**(27), 6669–6679 (2007).
8. A. Soubret, J. Ripoll, and V. Ntziachristos, "Accuracy of fluorescent tomography in the presence of heterogeneities: study of the normalized born ratio," *IEEE Trans. Med. Imaging* **24**(10), 1377–1386 (2005).
9. D. Wang et al., "A novel finite-element-based algorithm for fluorescence molecular tomography of heterogeneous media," *IEEE Trans. Inf. Technol. Biomed.* **13**(5), 766–773 (2009).
10. D. Hyde et al., "Data specific spatially varying regularization for multimodal fluorescence molecular tomography," *IEEE Trans. Med. Imaging* **29**(2), 365–374 (2010).
11. M. C. Pierce et al., "Optical contrast agents and imaging systems for detection and diagnosis of cancer," *Int. J. Cancer* **123**(9), 1979–1990 (2008).
12. E. Graves, R. Weissleder, and V. Ntziachristos, "Fluorescence molecular imaging of small animal tumor models," *Curr. Mol. Med.* **4**(4), 419–430 (2004).
13. N. C. Deliolanis et al., "In-vivo imaging of murine tumors using complete-angle projection fluorescence molecular tomography," *J. Biomed. Opt.* **14**(3), 030509 (2009).
14. M. Rudin and R. Weissleder, "Molecular imaging in drug discovery and development," *Nat. Rev. Drug Discov.* **2**, 123–131 (2003).
15. X. Cao et al., "Accelerated image reconstruction in fluorescence molecular tomography using dimension reduction," *Biomed. Opt. Exp.* **4**(1), 1–14 (2013).
16. X. Liu et al., "Unmixing dynamic fluorescence diffuse optical tomography images with independent component analysis," *IEEE Trans. Med. Imaging* **30**(9), 1591–1604 (2011).
17. X. Liu et al., "Principal component analysis of dynamic fluorescence diffuse optical tomography images," *Opt. Exp.* **18**(6), 6300–6314 (2010).
18. B. Alacam and B. Yazici, "Direct reconstruction of pharmacokinetic rate images of optical fluorophores from NIR measurements," *IEEE Trans. Med. Imaging* **28**(9), 1337–1353 (2009).
19. B. Alacam et al., "Pharmacokinetic-rate images of indocyanine green for breast tumors using near-infrared optical methods," *Phys. Med. Biol.* **53**(4), 837–859 (2008).
20. S. V. Patwardhan et al., "Time-dependent whole-body fluorescence tomography of probe bio-distributions in mice," *Opt. Exp.* **13**(7), 2564–2577 (2005).
21. V. Saxena, M. Sadoqi, and J. Shao, "Indocyanine green-loaded biodegradable nanoparticles: preparation, physicochemical characterization, and in vitro release," *Int. J. Pharm.* **278**(2), 293–301 (2004).
22. E. M. C. Hillman and A. Moore, "All-optical anatomical co-registration for molecular imaging of small animals using dynamic contrast," *Nat. Photonics* **1**(9), 526–530 (2007).
23. V. Kolehmainen et al., "State-estimation approach to the nonstationary optical tomography problem," *J. Opt. Soc. Am. A* **20**(5), 876–889 (2003).
24. S. Prince et al., "Time-series estimation of biological factors in optical diffusion tomography," *Phys. Med. Biol.* **48**(11), 1491–1504 (2003).
25. M. Schweiger et al., "The finite element method for the propagation of light in scattering media: boundary and source conditions," *Med. Phys.* **22**(11), 1779–1792 (1995).
26. M. A. O'Leary, "Imaging with diffuse photon density waves," PhD Thesis, Univ. of Pennsylvania, Philadelphia (1996).

27. M. L. Landsman et al., "Light absorbing properties, stability, and spectral stabilization of indocyanine green," *J. Appl. Physiol.* **40**(4), 575–583 (1976).
28. X. Gao et al., "In vivo cancer targeting and imaging with semiconductor quantum dots," *Nat. Biotechnol.* **22**(8), 969–976 (2004).
29. S. R. Arridge, "Optical tomography in medical imaging," *Inverse Probl.* **15**, R41–R93 (1999).
30. P. K. Yalavarthy et al., "Structural information within regularization matrices improves near infrared diffuse optical tomography," *Opt. Exp.* **15**(13), 8043–8058 (2007).
31. C. C. Paige and M. A. Saunders, "LSQR: an algorithm for sparse linear equations and sparse least squares," *ACM Trans. Math. Software* **8**(1), 43–71 (1982).
32. J.-C. Baritoux et al., "Sparsity-driven reconstruction for FDOT with anatomical priors," *IEEE Trans. Med. Imaging* **30**(5), 1143–1153 (2011).
33. B. Dogdas et al., "Digimouse: a 3D whole body mouse atlas from CT and cryosection data," *Phys. Med. Biol.* **52**(3), 577–587 (2007).
34. D. Stout et al., "Creating a whole body digital mouse atlas with PET, CT and cryosection images," *Mol. Imaging Biol.* **4**(4), S27 (2002).
35. G. Alexandrakis, F. R. Rannou, and A. F. Chatziioannou, "Tomographic bioluminescence imaging by use of a combined optical-PET (OPET) system: a computer simulation feasibility study," *Phys. Med. Biol.* **50**(17), 4225–4241 (2005).
36. F. Liu et al., "A parallel excitation based fluorescence molecular tomography system for whole-body simultaneous imaging of small animals," *Ann. Biomed. Eng.* **38**(11), 3440–3448 (2010).
37. J. T. Elliott et al., "Model-independent dynamic constraint to improve the optical reconstruction of regional kinetic parameters," *Opt. Lett.* **37**(13), 2571–2573 (2012).
38. S. C. Davis et al., "Dynamic dual-tracer MRI-guided fluorescence tomography to quantify receptor density in vivo," *Proc. Natl. Acad. Sci. U. S. A.* **110**, 9025–9030 (2013).

Wei He received a BS degree in biomedical engineering from Hebei University of Technology, Tianjin, China, in 2008 and received an MS degree in mechanical engineering from China Agricultural University, Beijing, China, in 2010. Currently, he is a PhD candidate in the Department of Biomedical Engineering, Tsinghua University, Beijing, China. His research interests focus on fluorescence molecular tomography for small animal imaging.

Guanglei Zhang received an MS degree in biomedical engineering from Northwestern Polytechnical University, Xi'an, China, in 2007.

Currently, he is a PhD candidate in the Biomedical Engineering Department, Tsinghua University, Beijing, China. His research interests focus on fluorescence molecular tomography for small animal imaging.

Huangsheng Pu received an MS degree in biomedical engineering from Fourth Military Medical University, Xi'an, China, in 2010. He is currently a PhD candidate in the Biomedical Engineering Department, Tsinghua University, Beijing, China. His research interest is inverse problems of fluorescence molecular tomography.

Fei Liu received a BS degree in biomedical engineering from Zhejiang University, Zhejiang, China, in 2008 and a PhD degree in biomedical engineering from Tsinghua University, Beijing, China, in 2013. She is currently a postdoctoral fellow in the Biomedical Engineering Department, Tsinghua University, Beijing, China. Her research interest is fluorescence molecular tomography for small animal imaging.

Xu Cao received a BS degree in biomedical engineering from Northwest Polytechnical University, Xi'an, China, in 2007 and received a PhD degree in the Biomedical Engineering Department, Tsinghua University, Beijing, China, in 2013. Now, he is a lecturer in the School of Life Sciences and Technology, Xidian University, Xi'an, China. His research interest is the optical molecular imaging.

Jianwen Luo received his BS and PhD degrees in biomedical engineering from Tsinghua University in 2000 and 2005, respectively. He was a postdoctoral research scientist from 2005 to 2009, and an associate research scientist from 2009 to 2011, in the Department of Biomedical Engineering at Columbia University. He became a professor at Tsinghua University in 2011 and was enrolled in the Thousand Young Talents Program in 2012. His research interest is biomedical imaging.

Jing Bai received an MS and a PhD degree from Drexel University, in 1983 and 1985, respectively. From 1985 to 1987, she was a research associate and assistant professor at the Biomedical Engineering and Science Institute, Drexel University. In 1991, she became a professor in the Biomedical Engineering Department of Tsinghua University. Her current research interests include medical ultrasound and infrared imaging. She has authored or coauthored ten books and more than 300 journal papers.